X-ray properties of $z > 4$ blazars

L. Ighina,[1,2]★ A. Caccianiga ⬝,[1] A. Moretti,[1] S. Belladitta,[1,3] R. Della Ceca,[1] L. Ballo ⬝[4]
and D. Dallacasa[5,6]

[1]*INAF - Osservatorio Astronomico di Brera, via Brera 28, I-20121 Milano, Italy*
[2]*Dipartimento di Fisica G. Occhialini, Università di Milano-Bicocca, Piazza della Scienza 3, I-20126 Milano, Italy*
[3]*DiSAT, Università degli Studi dell'Insubria, Via Valleggio 11, I-22100 Como, Italy*
[4]*XMM-Newton Science Operations Centre, ESAC/ESA, PO Box 78, Villanueva de la Cañada, E-28691 Madrid, Spain*
[5]*Dipartimento di Astronomia, Università di Bologna, via Ranzani 1, I-40127 Bologna, Italy*
[6]*INAF - Istituto di Radioastronomia, via Gobetti 101, I-40129 Bologna, Italy*

ABSTRACT

We present the X-ray analysis of the largest flux-limited complete sample of blazar candidates at $z > 4$ selected from the Cosmic Lens All Sky Survey (CLASS). After obtaining a nearly complete (24/25) X-ray coverage of the sample (from Swift-XRT, *XMM–Newton*, and *Chandra*), we analysed the spectra in order to identify the bona fide blazars. We classified the sources based on the shape of their Spectral Energy Distributions and, in particular, on the flatness of the X-ray emission and its intensity compared to the optical one. We then compared these high-z blazars with a blazar sample selected at lower redshifts ($\bar{z} \sim 1$). We found a significant difference in the X-ray-to-radio luminosity ratios, with the CLASS blazars having a mean ratio 2.4 ± 0.5 times larger than low-z blazars. We tentatively interpret this evolution as due to the interaction of the electrons of the jet with the Cosmic Microwave Background photons, which is expected to boost the observed X-ray emission at high redshifts. Such a dependence has been already observed in highly radio loud AGNs in the recent literature. This is the first time it is observed using a statistically complete radio flux limited sample of blazars. We have then evaluated whether this effect could explain the differences in the cosmological evolution recently found between radio and X-ray selected samples of blazars. We found that the simple version of this model is not able to solve the tension between the two evolutionary results.

Key words: galaxies: active – galaxies: high-redshift – galaxies: nuclei – X-rays: general.

1 INTRODUCTION

The detection and the study of very high redshift active galactic nuclei (AGNs) is the best way to provide observational constraints to current theoretical models of supermassive black holes growth from primordial seed BHs (e.g. Volonteri 2010). However, the number of high-z AGNs observed could be largely affected by obscuration effects which are difficult to quantify (e.g. Zeimann et al. 2011). This produces a systematic uncertainty in the statistical estimates due to the assumptions made about the absorbed population. This is why, in the last years, the class of blazars has acquired a particular importance (e.g. Volonteri et al. 2011 and Sbarrato et al. 2015). These objects are radio loud (RL[1]) AGNs whose relativistic jet points directly towards us, making obscuration less important,

because we are observing them roughly perpendicularly to the dusty torus. At the same time, from the number of observed blazars it is possible to infer the total density of RL AGNs with similar properties at a given redshift ($N_{tot} \approx N_{obs} \times 2\Gamma^2$; e.g. Ghisellini et al. 2014).[2] This estimate is potentially free from the usual bias due to the obscuration and, therefore, it complements the independent estimates based on non-blazar AGNs. However, for a correct application of this method it is fundamental to have a reliable procedure to distinguish blazars from non-blazar sources.

To date the largest flux-limited sample of blazar candidates at redshift larger than four has been derived from the CLASS survey (26 sources; Caccianiga et al. 2019, hereafter C19). From the analysis of their radio spectra, C19 identified the 18 bona-fide blazars (i.e. those with a flat radio spectrum) and then derived, for the first time, the density distribution of blazars at $z > 4$. Nevertheless,

---

★ E-mail: l.ighina@campus.unimib.it
[1]i.e. with a radio loudness $R > 10$, where $R = (f_{5\,GHz}/f_{4400\,Å})$, Kellermann et al. (1989).

[2]Where Γ is the bulk Lorentz factor of the plasma within the jet. Typically $\Gamma \sim 10$–15 (e.g. Ghisellini et al. 2010).

the analysis of the radio spectra alone is not 100 per cent reliable in the recognition of all the blazar sources in a sample. As discussed by C19, for instance, there is at least one striking case of high-z quasar (QSO) (J090631+693027, at z = 5.47; Romani et al. 2004), that shows a peaked radio spectrum, apparently not supporting a blazar classification. However, several pieces of evidence, based on very long baseline interferometer (VLBI) data (Coppejans et al. 2017), variability arguments, and on the shape of the spectral energy distribution (SED), have clearly revealed the blazar nature of this object (see discussion in C19). This demonstrates that the analysis of the radio spectra can provide a simple tool to quickly classify the sources in large samples, but it can miss a fraction of blazars. An X-ray analysis can provide a more accurate tool to discriminate blazars from non-blazars. Indeed, as described in the following sections, blazars are characterized by a strong, with respect to the optical, and flat X-ray emission which, combined with the other pieces of information, can then be used for a more reliable classification. In this paper we present the analysis of the X-ray observations of the CLASS sample together with their classification (blazar versus non-blazar).

In addition, a systematic study of the X-ray properties of the CLASS high-z blazars can help to understand the discrepancy found between the cosmological evolution of the radio-selected blazars at $z > 4$ and the X-ray selected ones. In particular, in C19, we found that the space density of the blazars with a radio luminosity between $\sim 10^{43}$ and $3 \times 10^{44}\,\mathrm{erg\,s^{-1}}$ (at 1.4 GHz) is in good agreement with the predictions recently presented by Mao et al. (2017), suggesting a peak at redshift ~ 2. This is significantly different from what has been found by Ajello et al. (2009) using an X-ray selected sample of blazars and that suggests a much higher redshift peak ($z \sim 4$). If the average X-ray-to-radio luminosity ratio in blazars is constant along the cosmic time, the observed differences are difficult to explain. On the contrary, a dependence of this luminosity ratio with redshift could, in principle, reconcile the two results. For this reason, in this paper we will use the results of our X-ray analysis to compare the X-ray-to-radio luminosity ratio of the high-z blazars in CLASS with a reference sample selected at lower redshift, searching for any possible dependence.

This paper is organized as follows: in Section 2 we summarize the selection criteria of the CLASS sample, while in Section 3 we report the X-ray observations of the sources and their analysis. The SED of each source is reported in Section 4. In Section 5 we use the results of the analysis to identify the blazar-like objects and in Section 6 we compare their X-ray and radio properties with low-z blazars. Finally, in Section 7 we summarize our results.

Through this paper we assume a flat ΛCDM cosmology with $H_0 = 70\,\mathrm{km\,s^{-1}\,Mpc^{-1}}$, $\Omega_\Lambda = 0.7$, $\Omega_M = 0.3$. Spectral indexes are given assuming $S_\nu \propto \nu^{-\alpha}$. All the errors are reported at 90 per cent confidence level, unless otherwise specified.

2 THE CLASS SAMPLE OF HIGH REDSHIFT BLAZARS

All the sources analysed in this work have been selected from the CLASS survey (Browne et al. 2003; Myers et al. 2003), a density flux limited survey ($S_{5\,\mathrm{GHz}} > 30\,\mathrm{mJy}$) of flat spectrum radio sources, which covers most of the northern sky ($16\,300\,\mathrm{deg}^2$) and that contains more than 11 000 objects (see Fig. 1). It was built by combining the NRAO VLA Sky Survey (NVSS) at 1.4 GHz (Condon et al. 1998) with the Green-Bank Survey (GB6) at 5 GHz (Gregory et al. 1996) and by selecting only those objects with a flat ($-0.5 < \alpha < 0.5$) spectrum between 1.4 and 5 GHz.
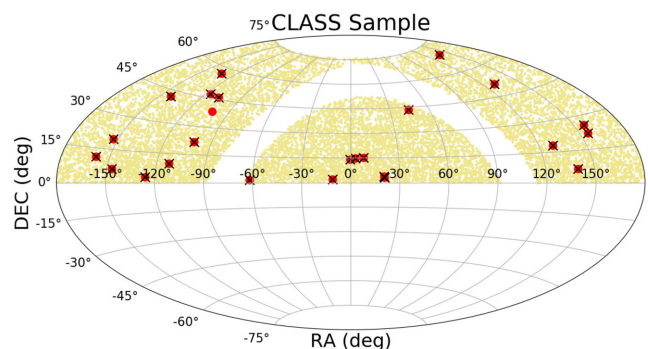

Figure 1. Sky coverage of the CLASS survey (yellow points). We report in red the $z > 4$ sources confirmed by C19 and with the black crosses those sources for which X-ray data are available.

The selection of the high-z sources in the CLASS survey has been described in details in C19. Here we summarize the main steps. The optical counterparts of the CLASS sample have been searched using the Panoramic Survey Telescope and Rapid Response System (Pan-STARRS1, PS1; Chambers et al. 2016) an optical survey in five different filters (g, r, i, z, Y), within a search radius of 0.6 arcsec from the radio position. Then, we have used the PS1 photometric data and the *dropout* method to efficiently pre-select objects at high redshift ($4 < z < 6$). In order to confirm the high-z nature of these selected objects we have carried out a systematic spectroscopic follow-up. In particular, all the candidates without an archival optical spectrum were observed at the Large Binocular Telescope (LBT) or at the Telescopio Nazionale Galileo (TNG), providing a spectroscopic estimate of the redshift for all the sources.

Most of the observed objects were confirmed as high-z AGN leading to a final sample of 26 confirmed $z > 4$ AGNs. However, after the publication of C19, we discovered that one of the sources (GB6J160608+312504) has an incorrect spectroscopic redshift reported in the literature (see Belladitta et al. 2019, for further information). For this reason, we do not consider that object in this work, reducing the sample to 25 sources (see red dots in Fig. 1). In C19 we extended the range of radio frequencies used to define the CLASS survey to refine the spectral classification of each high-z object, keeping as blazars only the 18 sources with a flat spectrum between 150 MHz up to 8.4 GHz (observed frame). The remaining objects show a possibly peaked spectrum that does not support their blazar nature. However, as already pointed out, some blazars can show a peaked spectrum. This is in part due to the non-simultaneous radio data used for the classification that may lead to mis-classify a variable blazar as non-flat source. In addition, there is at least one known case of a blazar (the already mentioned J090631+693027) that shows a peaked radio spectrum even using simultaneous radio data. It is also known that flaring blazars may temporarily show a peaked spectrum, like the High Frequency Peakers (Orienti, Dallacasa & Stanghellini 2007, 2010). The X-ray analysis discussed in the next sections will help us to derive a firmer classification of all the 25 high-z blazar candidates.

3 X-RAY SPECTRAL ANALYSIS

Out of the 25 high-z sources in the CLASS sample, 16 have X-ray data available in the public archives of *XMM–Newton*, *Chandra*, and *Swift-XRT*. In order to complete the X-ray coverage of the sample, we carried out a dedicated *Swift-XRT* follow-up of the remaining

Table 1. X-ray observations of the CLASS sample.

Name	z	Coordinates (J2000.0)	X-ray Telescope	Observation ID	Observation Date	Exp. time (ks)	Ref.
GB6J001115+144608	4.96	00 11 15.24 +14 46 01.8	*Chandra*	3957	2003/05	3.49	3
			XMM	0600090101	2010/01	29.20	8
GB6J003126+150729	4.29	00 31 26.80 +15 07 39.5	*Chandra*	18442	2016/06	5.35	2
GB6J012126+034646	4.13	01 21 26.15 +03 47 06.7	*Chandra*	3151	2002/02	5.68	1,7
			XMM	0200730301	2004/01	21.60	4
GB6J012202+030951	4.00	01 22 01.91 +03 10 02.4	*Swift*	00035924	2007/06 - 2008/01	4.03	–
			Swift	00036780	2008/01	4.65	–
GB6J025758+433837	4.07	02 57 59.08 +43 38 37.7	*Chandra*	18449	2015/12	5.51	2
GB6J083548+182519	4.41	08 35 49.43 +18 25 20.1	*Swift*	00087221	2017/01-02-05	49.50	2
GB6J083945+511206	4.40	08 39 46.22 +51 12 02.8	*Chandra*	3562	2004/01	4.9	5,8,9
			Swift	00515375	2012/02	29.75	5
			XMM	0650340201	2011/04	9.90	–
			XMM	0301340101	2006/04	4.90	8
GB6J090631+693027	5.47	09 06 30.75 +69 30 30.8	*Chandra*	5637	2005/07	29.79	1,10
			Swift	00035974	2006/10 - 2014/02	30.46	–
			Swift	00035369	2006/01-05-06	5.90	–
GB6J091825+063722	4.22	09 18 24.38 +06 36 53.4	*Chandra*	3563	2002/12	4.90	5,9
GB6J102107+220904	4.26	10 21 07.58 +22 09 21.6	*XMM*	0406540401	2016/11	22.70	2
GB6J102623+254255	5.28	10 26 23.62 +25 42 59.4	*Chandra*	12167	2012/03	4.99	1
			Swift	000325000	2012/06	10.11	6
GB6J132512+112338	4.42	13 25 12.49 +11 23 29.8	*Chandra*	3565	2003/03	4.70	1,9
GB6J134811+193520	4.40	13 48 11.26 +19 35 23.5	*Swift*	00087542	2017/11-12 - 2018/01	46.79	2
GB6J141212+062408	4.47	14 12 09.97 +06 24 06.8	*Chandra*	12169	2011/03	4.1	1
			Swift	00085421	2014/04-05-06-08-12	26.38	–
GB6J143023+420450	4.72	14 30 23.74 +42 04 36.5	*Chandra*	7874	2007/03	10.57	11
			Swift	00080752	2014/07	9.61	–
			Swift	00036798	2013/11-12	4.27	–
			XMM	0212480701	2005/06	11.00	1,12
			XMM	0111260101	2002/12	9.90	13,14
			XMM	0111260701	2003/01	11.50	14,15
GB6J151002+570256	4.31	15 10 02.93 +57 02 43.4	*Chandra*	2241	2001/06	88.98	1,16,17
			XMM	0111260201	2002/05	8.70	13,15,18
GB6J153533+025419	4.39	15 35 33.88 +02 54 23.4	*Swift*	00087222	2016/12 - 2017/01	26.40	2
GB6J161216+470311	4.36	16 12 16.76 +47 02 53.6	*Swift*	00087543	2017/11-12	48.68	2
GB6J162956+095959	5.00	16 29 57.28 +10 00 23.5	*Swift*	03109568	2019/02-03-04-05-06	18.10	–
GB6J164856+460341	5.36	16 48 54.53 +46 03 27.4	*Swift*	00010651	2018/04	14.40	–
GB6J171521+214547	4.01	17 15 21.25 +21 45 31.7	*Chandra*	4815	2004/06	9.54	1,7
GB6J195135+013442	4.11	19 51 36.02 +01 34 42.7	*Swift*	00036263	2007/03	10.23	1,19
GB6J231449+020146	4.11	23 14 48.71 +02 01 51.1	*Chandra*	18448	2016/01	5.88	2
			Swift	00085422	2014/11 - 2015/01-04-05	24.90	–
GB6J235758+140205	4.35	23 57 58.56 +14 02 01.9	*Swift*	00087544	2017/11-12 - 2018/01	34.10	–

Note. All the sources composing the CLASS sample for which X-ray observations are available, with their redshift and sky coordinates. For each observation we report the satellite, the identification number, the observation date, and the exposure time. The last column reports other works where the X-ray observations have also been analysed: 1 = Wu et al. (2013), 2 = Zhu et al. (2019), 3 = Shemmer et al. (2006), 4 = Shemmer et al. (2005), 5 = Sbarrato et al. (2013), 6 = Sbarrato et al. (2012), 7 = Vignali et al. (2003), 8 = Saez et al. (2011) 9 = Bassett et al. (2004), 10 = Romani et al. (2004), 11 = Cheung et al. (2012) , 12 = Eitan & Behar (2013), 13 = Grupe et al. (2006), 14 = Worsley et al. (2004), 15 = Page et al. (2005), 16 = Siemiginowska et al. (2003), 17 = Yuan et al. (2003), 18 = Yuan et al. (2006), 19 = Healey et al. (2008).

nine objects. Only one of them (GB6J171103+383016) has not been observed yet and, therefore, it will not be included in this work. To date we have X-ray data for 24 high-z objects (see Table 1 and black crosses in Fig. 1).

In order to have a systematic and up-to-date analysis of the entire sample, we carried out the X-ray analysis of all the sources, both the newly observed and the ones already discussed in the literature.

Data of the *Swift-XRT telescope* (Burrows et al. 2005) were downloaded from HEASARC public archive. They were then processed with the specific Swift software included in the package HEASOFT (v. 6.23, Evans et al. 2009). Chandra observations, made through the Advanced CCD Imaging Spectrometer (ACIS; Garmire

et al. 2003), were reduced using the software CIAO (v4.6[3]). Source and background counts were extracted using SPECEXTRACT, where the two regions consisted in circles of radii ∼2 and ∼30 arcsec, respectively, with all the background regions, chosen close to the target, not containing other X-ray sources. For *XMM* observations we only considered the data from the PN detector[4] (Pietsch et al.

---

[3]We checked that the results obtained with the latest version (v4.11) do not differ from ours.

[4]We did not consider the data from the MOS detectors since the EPIC-pn observations alone provided enough photon counts for the purposes of our analysis.
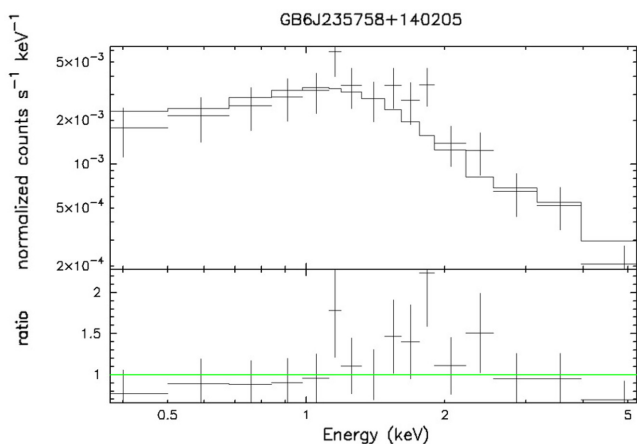
Figure 2. Top panel: *Swift-XRT* X-ray spectrum of GB6J235758+140205, example of a good blazar candidate. The model used is a Galactic absorbed power law with parameters: $N_H = 3.41 \times 10^{20}$ cm^{-2} and $\Gamma = 1.50 \pm 0.18$. Bottom panel: ratio between the data and the model.

2003), which were reduced through standard *XMM–Newton* Science Analysis System (SAS; v.17.0) routine. The photon counts this time have been extracted from a circle of radius ~40 arcsec for the targets and from a nearby circle of radius ~100 arcsec source-free. For all the observations the source regions have been centred in the peak of the X-ray emission.

We performed the X-ray spectral analysis for each observation independently using the package xspec (v.12.9.0i) and by fitting the observed spectra with a simple power law absorbed by the Galactic column density along the line of sight. As an example, we report in Fig. 2 the X-ray spectrum of the source GB6J235758+140205, a good blazar candidate. We do not consider intrinsic absorption at the source redshift since, usually, blazars do not show evidence of a significant absorption (e.g. Giommi et al. 2019, but see Eitan & Behar 2013 and Saez et al. 2011 for the discussion of some exceptions). In any case, the available statistics is in general too limited to attempt a search of any extra absorption in our targets and, for the few sources with enough counts, the addition of an extra component in the fitting model does not affect the analysis.

For the objects with more than 40 net counts, after grouping them in bins of energy with at least 10 counts each, we used the χ^2 statistics to derive the best-fit, whereas for those sources with a limited number of photon counts ($\lesssim$40, 11 observations), where an efficient grouping was not possible, we performed the fit using the C-statistic (Cash 1979) on the data. In Table 2 we report the results of the fit, together with the 90 per cent confidence range for the photon indexes and the observed fluxes. The flux error has been computed considering both the uncertainty on the photon index[5] and the Poissonian error associated to the photon counts.

For the objects already published we found a good agreement, in general, between our results and those found in the literature (see Table 2). For about 40 per cent of the sample, we analysed multiple observations and, even though blazars are known to be highly variable in the X-rays (e.g. Giommi et al. 2019), we decided to combine their best-fitting values with a weighted average, because there are no striking evidences of variability in our data. The

only source that presents a significant variability between different observations is GB6J143023+420450, which has already been deeply studied in the literature (e.g. Worsley et al. 2004 and Page et al. 2005). For simplicity, however, in the following paragraphs we use the analysis of the combined spectrum also for this object, since we verified that even in this case the main results discussed here would not change.

In Fig. 3 we report the photon index versus the X-ray luminosity ([2–10] keV rest frame) obtained from the analysis for the majority (~80 per cent) of the sources in the sample, i.e. those with a photon index uncertainty <0.5. Our sample presents an overall average photon index ($\bar{\Gamma} = 1.41^{+0.30}_{-0.28}$, red line) significantly flatter than the average value found in Shemmer et al. (2005) for a sample of radio-quiet (RQ) AGNs at $z > 4$ (green dashed line), supporting the idea that the majority of the sources selected in C19 are indeed blazars.

4 SPECTRAL ENERGY DISTRIBUTIONS

In this section we report and discuss all the rest-frame Spectral Energy Distributions (SEDs) of the CLASS sources. They have been built by combining multiwavelength observations from the radio up to X-ray band. X-ray data are the ones analysed in this work, whereas other photometric points have been taken from different surveys:

(i) **Radio**: The Giant Metrewave Radio Telescope (GMRT) all-sky survey (150 MHz; Intema et al. 2017), NVSS (1.4 GHz), GB6 (5 GHz), and Very Large Array (VLA, 8.4 GHz);

(ii) **Infra-Red**: *Wide-field Infrared Survey Explorer* (*WISE*; Wright et al. 2010) with the four filters *W*1, *W*2, *W*3, *W*4 (3.4, 4.6, 12, and 22 µm respectively). Five of our sources have not been detected in this survey;

(iii) **Optical**: Pan-STARRS1, with the filters *g*, *r*, *i*, *z*, *Y*, (4866–9633 Å);

(iv) **Multiwavelength**: data points taken from the literature using the online tool SED builder[6] (grey points). They are mainly Sloan Digital Sky Survey (SDSS; York et al. 2000) and VLA Low-frequency Sky Survey Redux (VLSSr; Lane et al. 2014) observations.

We built the SED for all the objects in the sample (see Fig. 4) in order to visually show the intensity of the X-ray emission with respect to the optical/UV emission and to compare it to the emission expected for RL AGNs seen at large viewing angles (expected to be comparable to the RQ coronal emission, due to the de-beaming of the jet emission; e.g. Galbiati et al. 2005) with similar optical properties. Therefore, in all the SEDs we report the coronal X-ray luminosity expected in an AGN with similar optical properties following the relation found in Steffen et al. (2006) between the monochromatic luminosity at 2500 Å and the one at 2 keV (assuming a photon index: $\Gamma = 1.9$, continuous bright red line). The fading red region represents the 1σ uncertainty associated to this estimate, while the yellow column indicates the region with a significant dropout of the luminosity caused by the Lyman absorption (912–1216 Å).

The templates, in black, are taken from the SWIRE template library;[7] computed through the combination of the optical-IR spectra of an optically selected sample of type 1 QSO. In particular, we considered the three QSO templates available from the library

---

[5]We constrained the value of the photon index within the range $1 < \Gamma < 2.5$, since these are the limit values observed in flat radio spectrum quasars (FRSQs), e.g. Giommi et al. 2019.

[6]http://www.asdc.asi.it/articles.php?id = 11
[7]http://www.iasf-milano.inaf.it/~polletta/templates/swire_templates.html

Table 2. Results of the X-ray analysis.

Name	Obsid (Telescope)	Γ	F_x [0.5–10] keV	$log(L_x)$ [2–10] keV	χ^2 / d.o.f.
GB6J001115+144608	3957 (C)	$1.71^{+0.29}_{-0.29}$	$31.2^{+9.1}_{-7.6}$	46.48	7.9 / 6
	0600090101 (X)	$1.76^{+0.05}_{-0.05}$	$30.0^{+1.7}_{-1.6}$	46.49	71.6 / 75
GB6J003126+150729	18442 (C)	$2.50_{-0.59}$	$2.78^{+4.0}_{-1.4}$	45.61	19.1 / 12*
GB6J012126+034646	3151 (C)	$1.85^{+0.34}_{-0.33}$	$8.8^{+3.0}_{-1.5}$	45.83	2.2 / 3
	0200730301 (X)	$1.76^{+0.30}_{-0.27}$	$4.2^{+1.2}_{-0.5}$	45.50	10.8 / 7
GB6J012202+030951	00035924 (S)	$1.13^{+0.28}_{-0.29}$	$133.1^{+21.0}_{-34.6}$	46.61	0.8 / 4
	00036780 (S)	$1.20^{+0.25}_{-0.25}$	$149.2^{+28.1}_{-34.2}$	46.70	3.7 / 7
GB6J025758+433837	18449 (C)	$1.43^{+0.36}_{-0.35}$	$30.3^{+7.7}_{-6.9}$	46.15	1.8 / 6
GB6J083548+182519	00087221 (S)	$1.34^{+0.21}_{-0.21}$	$21.0^{+4.3}_{-4.1}$	46.00	3.9 / 6
GB6J083945+511206	3562 (C)	$1.65^{+0.31}_{-0.29}$	$14.4^{+3.8}_{-4.1}$	46.00	1.6 / 4
	00515375 (S)	$1.34^{+0.46}_{-0.46}$	$17.4^{+6.7}_{-6.8}$	45.92	3.8 / 3
	0650340201 (X)	$1.56^{+0.18}_{-0.16}$	$15.3^{+1.9}_{-2.0}$	45.98	10.6 / 11
	0301340101 (X)	$1.44^{+0.21}_{-0.20}$	$17.4^{+2.8}_{-3.1}$	45.98	16.9 / 20
GB6J090631+693027	5637 (C)	$1.51^{+0.12}_{-0.11}$	$15.7^{+1.6}_{-1.6}$	46.15	21.1 / 28
	00035974 (S)	$1.84^{+0.38}_{-0.34}$	$9.4^{+2.3}_{-1.5}$	46.12	5.2 / 4
	00035369 (S)	$1.01^{+0.62}_{-0.70}$	$23.4^{+6.0}_{-11.1}$	46.00	11.9 / 14*
GB6J091825+063722	3563 (C)	$1.26^{+0.35}_{-0.35}$	$14.7^{+4.4}_{-5.0}$	45.77	1.6 / 4
GB6J102107+220904	0406540401 (X)	$2.26^{+0.24}_{-1.64}$	$7.9^{+8.0}_{-1.3}$	46.00	5.5 / 6
GB6J102623+254255	12167 (C)	$1.29^{+0.34}_{-0.34}$	$13.0^{+3.3}_{-3.9}$	45.91	7.0 / 8
	00032500 (S)	$1.00^{+0.38}$	$14.9^{+3.5}_{-5.4}$	45.80	19.8 / 16*
GB6J132512+112338	3565 (C)	$1.52^{+0.51}_{-0.50}$	$6.5^{+4.4}_{-2.5}$	45.59	0.8 / 2*
GB6J134811+193520	00087542 (S)	$1.83^{+0.49}_{-0.55}$	$4.2^{+2.1}_{-0.8}$	45.55	3.7 / 2
GB6J141212+062408	12169 (C)	$1.57^{+0.70}_{-0.71}$	$6.4^{+4.9}_{-2.2}$	45.63	2.9 / 2*
	00085421 (S)	$1.59^{+0.80}_{-0.90}$	$4.4^{+2.7}_{-2.1}$	45.47	4.99 / 4*
GB6J143023+420450	7874 (C)	$1.33^{+0.05}_{-0.05}$	$235.1^{+11.6}_{-11.5}$	47.10	87.1 / 63
	00080752 (S)	$1.14^{+0.14}_{-0.14}$	$218.1^{+36.0}_{-38.5}$	46.95	7.2 / 13
	00036798 (S)	$1.21^{+0.18}_{-0.18}$	$219.6^{+29.4}_{-29.0}$	46.99	10.22 / 6
	0212480701 (X)	$1.49^{+0.04}_{-0.04}$	$180.0^{+5.4}_{-5.5}$	47.08	125.9 / 142
	0111260101 (X)	$1.75^{+0.14}_{-0.14}$	$202.7^{+20.6}_{-20.7}$	47.27	11.3 / 16
	0111260701 (X)	$1.67^{+0.04}_{-0.04}$	$169.0^{+4.7}_{-4.8}$	47.15	150.9 / 151
GB6J151002+570256	2241 (C)	$1.40^{+0.03}_{-0.03}$	$53.5^{+1.7}_{-1.7}$	46.40	387.6 / 200
	0111260201 (X)	$1.57^{+0.10}_{-0.09}$	$47.5^{+3.5}_{-3.6}$	46.47	121.2 / 102
GB6J153533+025419	00087222 (S)	$1.22^{+0.16}_{-0.16}$	$64.0^{+8.8}_{-9.1}$	46.44	10.4 / 14
GB6J161216+470311	00087543 (S)	$1.89^{+0.70}_{-0.66}$	$1.6^{+1.1}_{-0.7}$	45.15	1.36 / 4*
GB6J162956+095959	03109568(S)	$1.69^{+0.62}_{-0.67}$	$8.2^{+6.1}_{-3.1}$	45.90	3.06 / 4*
GB6J164856+460341	00010651 (S)	$1.09^{+1.69}_{-0.09}$	$3.1^{+1.5}_{-2.6}$	45.16	5.6 / 5 *
GB6J171521+214547	4815 (C)	$1.14^{+0.30}_{-0.30}$	$12.4^{+2.0}_{-3.6}$	45.59	6.7 / 6
GB6J195135+013442	00036263 (S)	$1.10^{+0.49}_{-0.50}$	$29.8^{+5.6}_{-9.6}$	45.96	1.4 / 3*
GB6J231449+020146	18448 (C)	$1.28^{+0.49}_{-0.51}$	$12.4^{+2.9}_{-4.7}$	45.68	3.2 / 3
	00085422 (S)	$1.86^{+0.67}_{-0.65}$	$3.5^{+1.9}_{-1.3}$	45.42	24.9 / 21*
GB6J235758+140205	00087544 (S)	$1.50^{+0.18}_{-0.18}$	$34.5^{+5.1}_{-5.6}$	46.30	11.5 / 14

Note. column 1: Object name; column 2: Obsid and the telescope (S = *Swift*, C = *Chandra*, X = *XMM*); columns 3: Photon index with its error. The best fit has been constrained to the interval [1–2.5]; column 4: X-ray observed flux in the energy range [0.5–10] keV, in units of 10^{-14} erg cm^{-2}s^{-1}, with its error; column 5: Logarithm of the rest-frame intrinsic Luminosity [2–10] keV in units of erg s^{-1}; column 6: Value of the χ^2 with the respective degrees of freedom. The "∗" sign indicates the observations where we adopted the C-statistic. In these cases the values reported correspond to the C-parameter (Cash 1979) and the degrees of freedom.
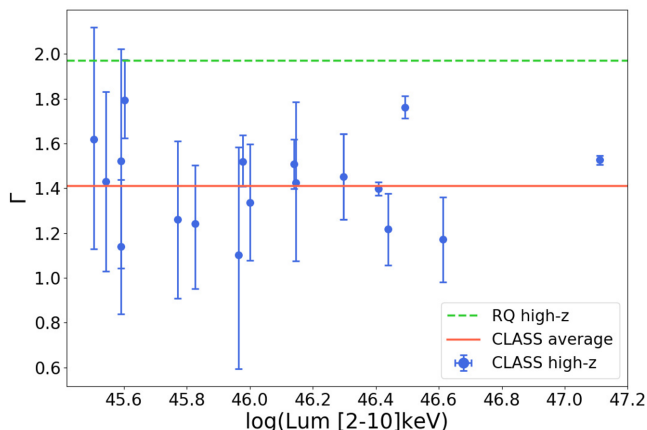
Figure 3. Photon index versus the rest-frame luminosity [2–10] keV for the sources of the CLASS sample with a reasonable estimate on the photon index (error < 0.5). The red line represents the average value of the CLASS sample, $\bar{\Gamma} = 1.41$, whereas the green dashed line is the average value of the sample of RQ AGNs discussed in Shemmer et al. (2005), $\bar{\Gamma} = 1.97$.

(QSO1, BSQO1, and TQSO1) characterized by different intensities of the infrared emission, and we chose the one that best represented the data.[8] The templates have been normalized in order to match the optical data points.

The X-ray data are represented with three different markers, corresponding to the telescope used for the observation (*Chandra* = green squares, *XMM* = purple triangles, *Swift* = blue diamonds), while radio, IR, and optical data are reported with brown pentagons. The two lines represent a power law connecting 2500 Å to 2 keV (orange dashed) and 10 keV (red continuous) rest-frame, respectively.

5 BLAZAR CLASSIFICATION

The α_{ox} parameter (Tananbaum et al. 1979) is commonly used in the literature in order to quantify the relative strength of the X-ray emission with respect to the optical/UV component. This parameter is the two-point spectral index of a fictitious power law connecting 2500 Å and 2 keV in the source rest frame. We report the value of the α_{ox} for the CLASS sample in Table 3 and, in the SEDs of Fig. 4, '1-α_{ox}' is reported as the slope of the orange dashed line. The luminosity at 2500 Å has been computed from the *i*-band magnitude (PS1) assuming an optical spectral index $\alpha_\nu = 0.46$ (Vanden Berk et al. 2001). Both the magnitude and the luminosity are also reported in Table 3.

Blazars and misaligned RL AGNs can be distinguished on the basis of the value of α_{ox}: sources with an X-ray emission strongly dominated by the relativistic jet will have a 'flat' α_{ox} index ($\lesssim 1.50$; Donato et al. 2001), while misaligned objects, where most of the observed X-ray emission is due to the corona, will have a steeper (i.e. higher) α_{ox} (~ 1.69; Shemmer et al. 2006). However, considering the monochromatic luminosity at 2 keV rest frame may not be the most convenient approach when dealing with high-z sources. Indeed, for objects with $z > 4$ this energy is observed at

~ 0.3–0.4 keV, where X-ray telescopes are less sensitive, making the estimate of the α_{ox} less accurate and highly dependent on the exact value of the spectral slope. For this reason we decided to consider the X-ray flux at higher energies, where the number of detected photons is larger and the normalization is less affected by a different photon index. To this end we introduce the parameter $\tilde{\alpha}_{ox}$, analogous to the α_{ox},[9] defined at 10 keV rest frame (in Fig. 4 '1-$\tilde{\alpha}_{ox}$' is reported as the slope of the continuous red line).

$$\tilde{\alpha}_{ox} = -\frac{\log(L_{10keV} / L_{2500\text{Å}})}{\log(\nu_{10keV} / \nu_{2500\text{Å}})} = -0.3026 \log(\frac{L_{10keV}}{L_{2500\text{Å}}}). \quad (1)$$

The second parameter we used for the blazar classification is the photon index. Indeed, we expect to observe different values of photon index, flat ($\lesssim 1.8$) for blazars and relatively steep (~ 1.9) for non-blazars (e.g. Giommi et al. 2019). We therefore used the two parameters, $\tilde{\alpha}_{ox}$ and Γ, for the blazar classification of the CLASS sources. In order to calibrate the classification of the sample, we decided to use two reference samples taken from the literature. As first sample, we selected all the FSRQs present in the 5th BZCAT edition (Massaro et al. 2015) with a radio flux density exceeding 1.5 Jy at 1.4 GHz. The reason for imposing the large flux limit is many-fold: first, at these flux levels, almost all of the blazars have already been discovered and, therefore, this can be confidently considered as a radio flux-limited sample (like CLASS). Secondly, the large majority of these objects has already been observed (and detected) in the X-rays. This is important to avoid the introduction of possible biases against X-ray weak blazars. For these reasons, this sample should be reasonably representative of the blazar population. Finally, with this flux limit we select objects in a similar range of radio power as the CLASS sources. To have an estimate of their X-ray slope and flux, we analysed all the *Swift-XRT* observations that are available for the majority (60 out of 105) of these blazars using the same model adopted for the CLASS, i.e. a Galactic absorbed power law. We then considered only the objects with an optical counterpart in the PS1 catalogue (47) in order to compute the $\tilde{\alpha}_{ox}$. The photon index as a function of the $\tilde{\alpha}_{ox}$ for these objects is reported in Fig. 5 (orange points). In this figure, we also report the few confirmed blazars at $z > 4$ with accurate determination of the X-ray parameters (taken from the literature) as red squares, together with the the best-fitting values of the faintest high-z ($z > 5$) blazar known so far, i.e. DESJ014132.4-542749.9 (Belladitta et al. 2019, red star). On the other hand, to have a term of comparison also for the coronal emission, we considered the sample of high redshift ($z > 4$) RQ AGNs discussed in Shemmer et al. (2005), since, as already mentioned, the X-ray-jet emission of RL AGNs is expected to be similar to RQ AGNs. Also in this case, we considered only the sources with an accurate estimate of the X-ray properties (photon index error < 0.3). These sources are reported in Fig. 5 as blue points. The continuous black line in Fig. 5 is the predicted dependence of the X-ray slope with the $\tilde{\alpha}_{ox}$ according to the beaming model and assuming that unbeamed objects have $\tilde{\alpha}_{ox} = 1.55$ and $\Gamma = 2$ while the jet has $\Gamma = 1.6$. The black cross indicates the critical angle that discriminates blazars from non-blazars ($1/\Gamma$, with Γ the bulk Lorentz factor of the jet), under the assumption that the intrinsic X-ray luminosity ratio (at 10 keV) between the blazar jet (viewing angle $\theta = 0$) and the corona is 50, similar to the maximal ratios observed in the CLASS sample (this critical angle can change with a different normalization). We have used a Lorentz factor of

---

[8]The plotted templates only serve as qualitative guide-lines to show the different components of the SED and they are not obtained through a proper fitting procedure. As described in the text, the quantitative analysis of the X-ray-to-optical luminosity ratio is done through the two-points spectral index (α_{ox})

[9]The two are related as follows: $\tilde{\alpha}_{ox} = 0.789\,\alpha_{ox} + 0.212\,\alpha$, with α the spectral index of the X-ray emission.
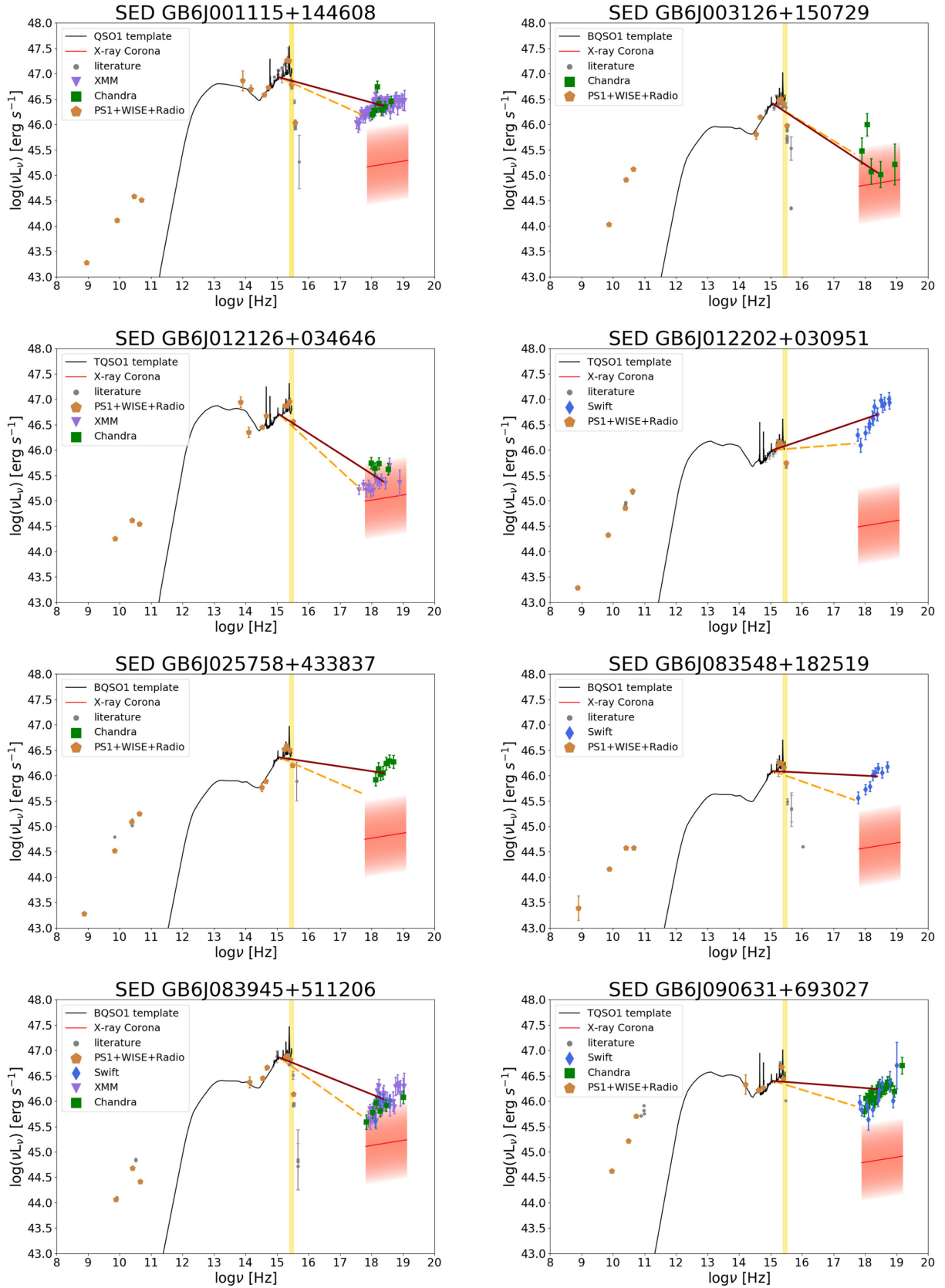
Figure 4. Broad-band SEDs of the sources of the CLASS sample discussed in this paper. In all the SEDs we report the expected X-ray coronal emission from an RQ AGN with similar optical luminosity (red region) and the spectral region where hydrogen absorption is relevant (yellow region). In this representation the plotted slopes of the dashed orange and the continuous red lines are equal to 1-α_{ox} and $1 - \tilde{\alpha}_{ox}$, respectively.
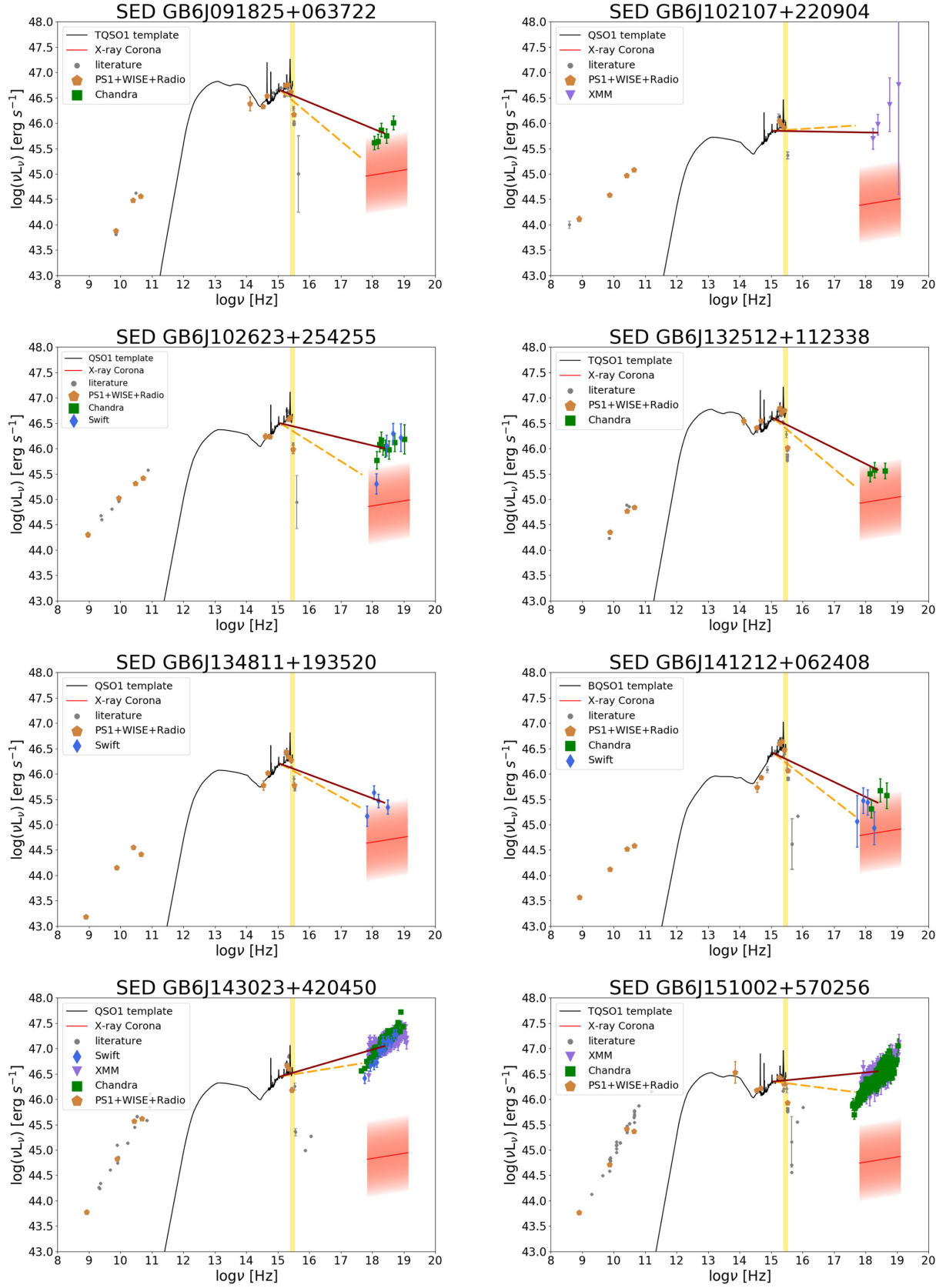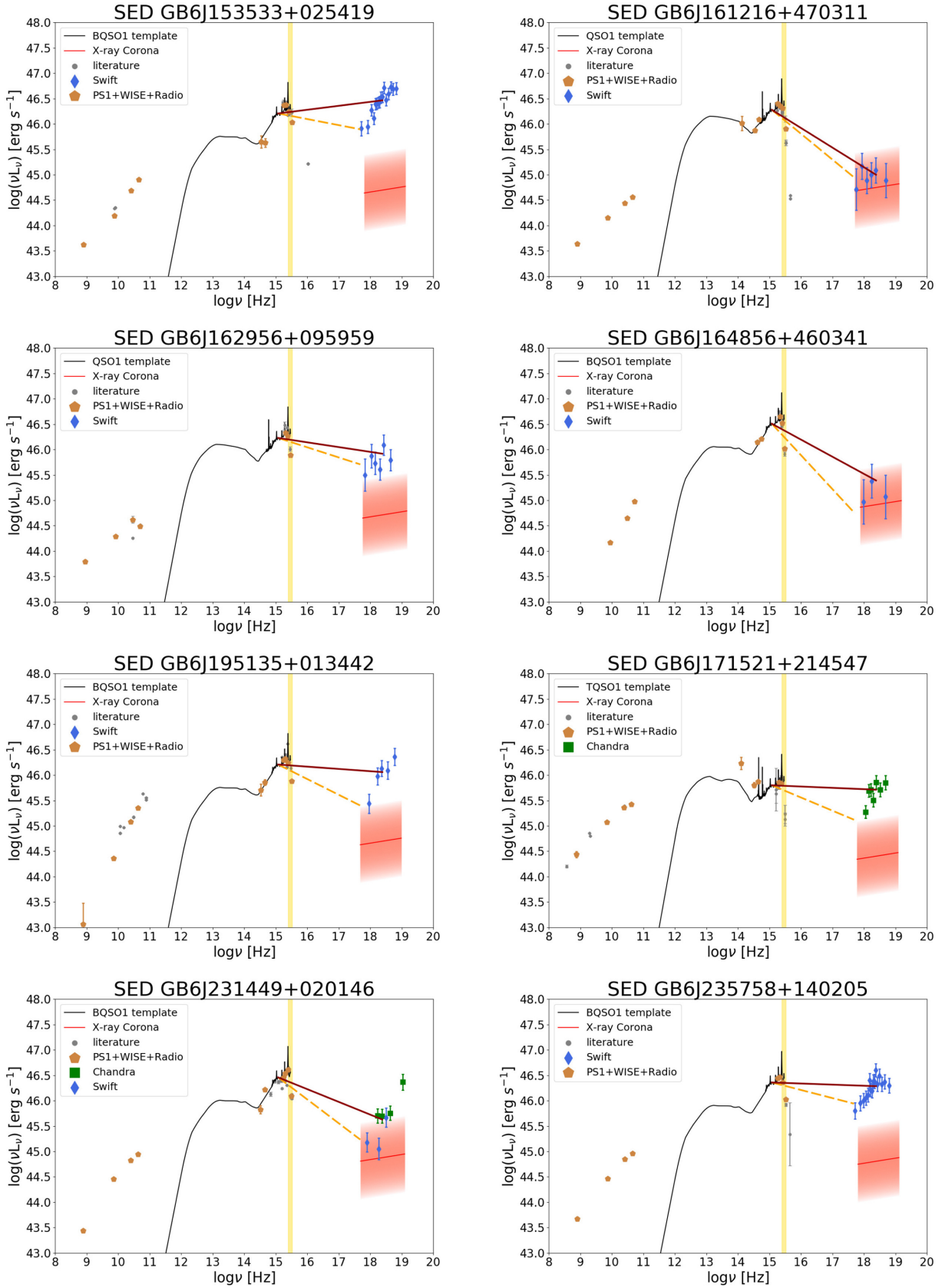
Figure 4. *– continued*

Figure 4. – *continued*

Table 3. Multiwavelength data of the CLASS sample, together with their X-ray and radio classification.

Name (1)	z (2)	N_H (3)	Γ (4)	α_r (5)	m_i (6)	$\log(L_{2500\text{Å}})$ (7)	$\log(R)$ (8)	α_{ox} (9)	$\bar{\alpha}_{ox}$ (10)	$\log(\frac{L_x}{L_R})$ (11)	X-ray class (12)	Radio class (13)
GB6J001115+144608	4.96	4.16	$1.76^{+0.05}_{-0.05}$	0.14	18.28 ± 0.01	32.02	2.09	$1.28^{+0.01}_{-0.01}$	$1.170^{+0.003}_{-0.002}$	3.05	Blazar	Flat?
GB6J003126+150729	4.29	3.86	$2.50_{-0.59}$	−0.53	19.79 ± 0.02	31.29	2.64	$1.38^{+0.15}_{-0.03}$	$1.404^{+0.003}_{-0.022}$	2.26	Non-Blazar	Flat
GB6J012126+034646	4.13	3.13	$1.80^{+0.18}_{-0.17}$	−0.88	18.76 ± 0.01	31.67	2.68	$1.57^{+0.03}_{-0.03}$	$1.409^{+0.018}_{-0.009}$	2.68	Non-Blazar	Peaked
GB6J012202+030951	4.00	3.06	$1.17^{+0.19}_{-0.19}$	−0.07	20.48 ± 0.03	30.96	3.42	$0.95^{+0.03}_{-0.04}$	$0.789^{+0.008}_{-0.013}$	3.05	Blazar	Flat
GB6J025758+433837	4.07	12.57	$1.43^{+0.36}_{-0.35}$	−0.28	19.45 ± 0.01	31.38	3.17	$1.27^{+0.10}_{-0.09}$	$1.093^{+0.011}_{-0.001}$	2.53	Blazar	Flat?
GB6J083548+182519	4.41	2.66	$1.34^{+0.21}_{-0.21}$	0.21	20.50 ± 0.04	31.03	3.18	$1.22^{+0.06}_{-0.05}$	$1.031^{+0.019}_{-0.011}$	2.42	Blazar	Flat
GB6J083945+511206	4.40	3.31	$1.52^{+0.12}_{-0.11}$	−0.47	18.88 ± 0.01	31.68	2.37	$1.44^{+0.02}_{-0.03}$	$1.247^{+0.005}_{-0.004}$	2.99	Blazar?	Peaked
GB6J090631+693027	5.47	3.74	$1.51^{+0.11}_{-0.11}$	< −0.82	20.54 ± 0.02	31.19	3.33	$1.19^{+0.03}_{-0.02}$	$1.048^{+0.005}_{-0.003}$	2.73	Blazar✓	Peaked
GB6J091825+063722	4.22	2.99	$1.26^{+0.35}_{-0.35}$	−0.17	19.09 ± 0.01	31.56	2.32	$1.52^{+0.07}_{-0.07}$	$1.257^{+0.022}_{-0.003}$	1.76	Blazar?	Flat
GB6J102107+220904	4.26	1.18	$2.26^{+0.24}_{-1.64}$	0.52	21.09 ± 0.06	30.76	3.89	$0.93^{+0.35}_{-0.01}$	$1.011^{+0.034}_{-0.007}$	2.10	Blazar	Flat
GB6J102623+254255	5.28	1.55	$1.24^{+0.26}_{-0.29}$	0.25	20.06 ± 0.02	31.35	3.74	$1.39^{+0.07}_{-0.06}$	$1.150^{+0.013}_{-0.002}$	1.40	Blazar✓	Flat
GB6J132512+112338	4.42	2.00	$1.52^{+0.51}_{-0.50}$	−0.59	19.36 ± 0.02	31.49	2.91	$1.52^{+0.12}_{-0.10}$	$1.308^{+0.031}_{-0.010}$	2.41	Blazar?	Peaked
GB6J134811+193520	4.40	1.91	$1.83^{+0.55}_{-0.49}$	0.00	20.26 ± 0.01	31.12	3.08	$1.34^{+0.13}_{-0.04}$	$1.232^{+0.086}_{-0.001}$	2.14	Blazar	Peaked
GB6J141212+062408	4.47	2.10	$1.62^{+0.49}_{-0.50}$	0.43	19.55 ± 0.04	31.42	2.75	$1.48^{+0.07}_{-0.08}$	$1.295^{+0.043}_{-0.048}$	1.81	Blazar?	Flat
GB6J143023+420450	4.72	1.18	$1.53^{+0.02}_{-0.02}$	−0.08	19.79 ± 0.04	31.37	3.35	$0.90^{+0.01}_{-0.01}$	$0.819^{+0.004}_{-0.004}$	3.10	Blazar✓	Flat
GB6J151002+570256	4.31	1.57	$1.40^{+0.03}_{-0.03}$	0.02	20.13 ± 0.02	31.16	3.56	$1.08^{+0.01}_{-0.01}$	$0.939^{+0.003}_{-0.003}$	2.40	Blazar✓	Flat
GB6J153533+025419	4.39	3.75	$1.22^{+0.16}_{-0.16}$	0.41	20.17 ± 0.04	31.16	3.06	$1.12^{+0.05}_{-0.04}$	$0.928^{+0.006}_{-0.005}$	2.68	Blazar	Flat
GB6J161216+470311	4.36	1.02	$1.89^{+0.70}_{-0.69}$	0.46	20.18 ± 0.02	31.15	3.11	$1.51^{+0.18}_{-0.12}$	$1.387^{+0.035}_{-0.002}$	1.65	Non-Blazar	Flat
GB6J162956+095959	5.00	4.71	$1.69^{+0.62}_{-0.67}$	0.49	20.77 ± 0.02	31.03	3.40	$1.20^{+0.19}_{-0.13}$	$1.094^{+0.036}_{-0.003}$	2.06	Blazar	Flat
GB6J164856+460341	5.36	1.51	$1.09^{+1.69}_{-0.09}$	−0.47	20.31 ± 0.02	31.27	2.86	$1.67^{+0.11}_{-0.31}$	$1.338^{+0.116}_{-0.002}$	2.19	Blazar?	Flat?
GB6J171521+214547	4.01	4.73	$1.14^{+0.30}_{-0.30}$	0.35	21.22 ± 0.05	30.66	4.53	$1.26^{+0.04}_{-0.06}$	$1.026^{+0.017}_{-0.006}$	0.98	Blazar	Flat
GB6J195135+013442	4.11	13.30	$1.10^{+0.50}_{-0.49}$	−0.33	20.14 ± 0.05	31.12	3.22	$1.31^{+0.05}_{-0.13}$	$1.045^{+0.009}_{-0.006}$	2.55	Blazar	Flat
GB6J231449+020146	4.11	4.72	$1.43^{+0.40}_{-0.40}$	−0.05	19.59 ± 0.01	31.34	3.21	$1.47^{+0.10}_{-0.09}$	$1.251^{+0.018}_{-0.006}$	1.83	Blazar	Peaked?
GB6J235758+140205	4.35	3.41	$1.50^{+0.18}_{-0.18}$	0.18	19.92 ± 0.03	31.25	3.28	$1.16^{+0.05}_{-0.04}$	$1.022^{+0.008}_{-0.003}$	2.43	Blazar	Flat

Note. column 1: Object name; column 2: Redshift; column 3: Galactic neutral hydrogen column density in unit of 10^{20} cm^{-2}; column 4: Photon Index between [0.5–10] keV. In case of multiple observations of the same source, we combined the different best-fitting values with a weighted average; column 5: Radio spectral index between 0.15 and 1.4 GHz (observed frame), with $S_\nu \propto \nu^{-\alpha}$; column 6: Apparent magnitude in the *i*-band (7545 Å) with its 1σ error from Pan-STARRS1; column 7: Logarithm of the monochromatic luminosity at 2500 Å rest frame in units of erg s^{-1} Hz^{-1}; column 8: Logarithm of the radio loudness R defined between 5 GHz and 4400 Å rest frame; column 9: Two point spectral index between 2500 Å and 2 keV rest-frame; column 10: Two point spectral index between 2500 Å and 10 keV rest frame; column 11: Logarithm of the rest-frame ratio between the X-ray [0.5–10] keV and the radio 1.4 GHz luminosities (νL_ν), both in in units of erg s^{-1}; column 12: X-ray classification of the sources discussed in this work. The sign '✓' shows the blazars already confirmed in the literature, whereas the sign '?' refers to an uncertain classification; column 13: Classification based on the radio spectrum between 0.15 and 8.4 GHz (observed frame) presented in C19. Also in this case the sign '?' denotes an uncertain classification.
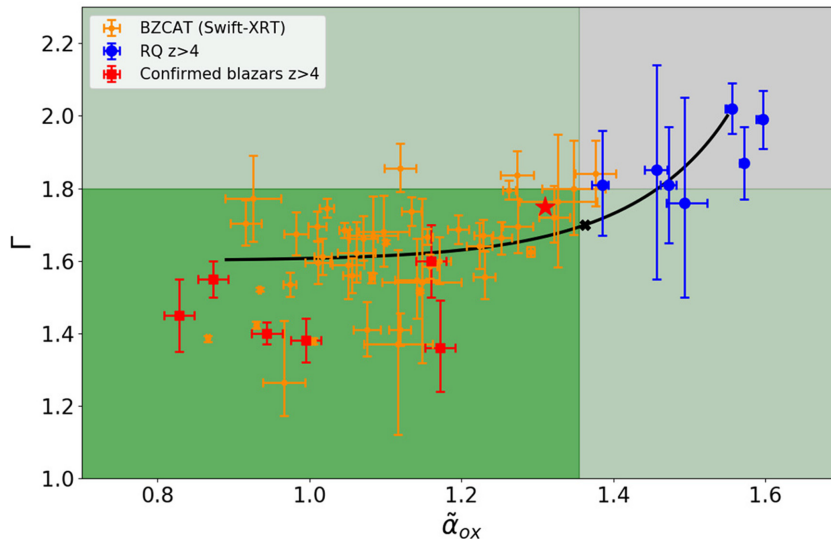
Figure 5. Photon index as a function of the $\tilde{\alpha}_{ox}$ index for the comparison samples. In orange we report the BZCAT blazars observed by *Swift-XRT*, with red squares the few confirmed blazars at high-z and with blue points the RQ AGNs at high-z. The red star represent the z = 5 blazar DESJ014132.4-542749.9, Belladitta et al. (2019). The continuous black line represents the dependence of the photon index with a variation of the X-ray intensity ($\tilde{\alpha}_{ox}$) of the jet due to beaming effects considering a coronal emission with $\tilde{\alpha}_{ox} = 1.55$ and $\Gamma = 2$, while for the jet emission we assume $\Gamma = 1.6$. The black cross represents the critical angle assuming that the jet seen at $\theta = 0$ is 50 times more intense than the corona at 10 keV. The plot is divided in four areas by a vertical line at $\tilde{\alpha}_{ox} = 1.355$ and a horizontal one at $\Gamma = 1.8$, which correspond to the thresholds assumed for the classification.

10, but there is very little dependence from the assumed value. The difference between the two populations is clear: RQ AGNs occupy only the top-right region of the plot, meaning that they have a weak and steep X-ray emission. On the other hand, most blazars have a stronger and flat emission and they are located in the bottom left-hand region. Based on this distinction, we set two thresholds to differentiate blazars and non-blazar AGNs. In particular, as shown in Fig. 5, we adopt the values $\Gamma = 1.8$ and $\tilde{\alpha}_{ox} = 1.355$ as thresholds to separate the two populations. These limits include all the confirmed high-z blazars. We then apply these criteria to the high-z AGN in the CLASS sample (Fig. 6). In particular, we plot here the 14 objects with a reasonable estimate of the photon index (error < 0.4). The remaining 10 will be discussed further below. The sources of our sample which have been already confirmed as blazars in the literature are highlighted by a black circle. In addition, in the plot it is also included the classification as blazar/non-blazars (flat/peaked) based on the radio spectrum and discussed in C19 (blue points = peaked, red squares = flat, and purple diamonds = uncertain).

Considering the objects plotted in Fig. 6, there is only one source whose Γ and $\tilde{\alpha}_{ox}$ are not consistent with a blazar nature (GB6J012126+034646), meaning that its X-ray spectrum is too steep and too weak to be produced by an oriented jet (grey region). On the other hand, as expected, the majority of the sources (13) are in the bottom left-hand region (green), meaning that they are strong and flat enough to suggest that they are bona fide blazars. Moreover, this method consistently classifies the already confirmed blazars at high redshift, including GB6J090631+693027 (discussed earlier), in spite having a peaked radio spectrum. For the remaining 10 sources of the sample, the X-ray analysis did not provide a photon index accurate enough to be used in the previous classification. In these cases we used only the information related to the X-ray intensity compared to the optical one ($\tilde{\alpha}_{ox}$) for the classification. In particular we considered as blazars the eight sources with an $\tilde{\alpha}_{ox}$ below the threshold ($\tilde{\alpha}_{ox} < 1.355$), while the candidates above the limit as non-blazars (two objects). The final results of the classification are reported in Table 3.

In summary, from this analysis a total of 21 objects are consistent with a blazar nature while the remaining three sources do not seem to be powered by a relativistic jet oriented towards us, corresponding respectively to ∼90 per cent and ∼10 per cent of the entire sample. There is only one source (GB6J164856+460341) that, even after the introduction of the new parameter, keeps a relatively large uncertainty on the X-ray intensity. Given the large uncertainty on the $\tilde{\alpha}_{ox}$ value and its proximity to the adopted threshold, we classify this object as 'blazar?'. Also its classification as 'flat radio source' is uncertain. A firm classification of this object is particularly interesting given its very high redshift ($z = 5.36$) that would make him the second most distant blazar discovered so far. We are observing this object with VLBI to secure a firmer classification.

This classification has a relatively good correspondence with the one based on the radio spectra from C19. In particular, the majority (∼90 per cent) of the candidates classified as blazars in C19 ('flat') has been confirmed also by the X-ray analysis. On the other hand, as mentioned before, there is a significant number of sources (5) that, like the blazar GB6J090631+693027, have a peaked radio spectrum, but the X-ray analysis suggests a blazar nature. We consider the X-ray classification more reliable and, for this reason, we adopted it in the analysis presented in the next sections.

6 X-RAY LUMINOSITY ENHANCEMENT

In this section we compare the X-ray-to-radio luminosity ratio (X/R ratio) of the high-z CLASS sources here classified as blazars, with the same blazar sample mentioned above (BZCAT; Massaro et al. 2015, $S_{1.4\,GHz} > 1.5$ Jy, $\bar{z} \sim 1.1$) , in order to find a possible dependence of this ratio on redshift. Fig. 7 reports the ratio of the integrated luminosity between [2–10] keV (energy band directly observed in both samples) and the radio luminosity at 1.4 GHz in the rest frame.
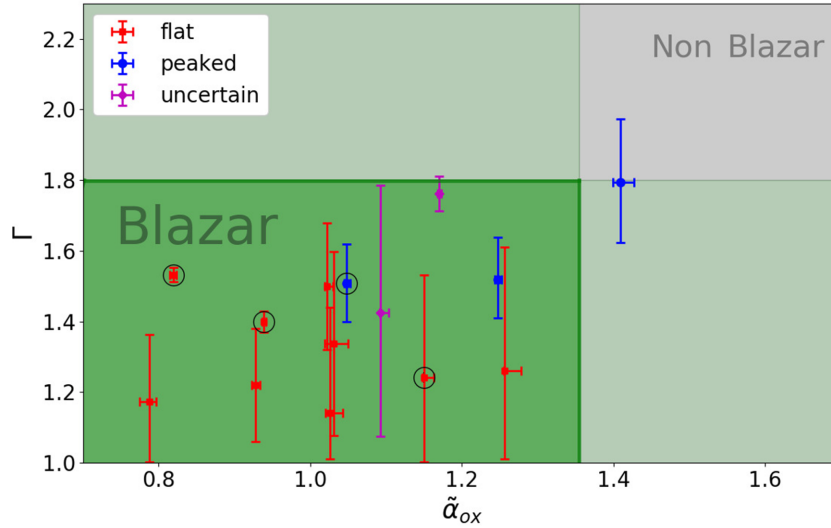
Figure 6. Photon index as a function of the $\tilde{\alpha}_{ox}$ for the high-z objects in the CLASS sample with an error on the photon index lower than 0.4. The objects are plotted with different colours and markers depending on the radio spectral classification reported in C19 ('flat' i.e. good blazar candidates, 'peaked' i.e. probably non-blazars and 'uncertain') and the black circles represent the few confirmed blazars at $z > 4$ in the literature. As in the previous figure, the plot is divided in four areas by a vertical line at $\tilde{\alpha}_{ox} = 1.355$ and a horizontal one at $\Gamma = 1.8$.
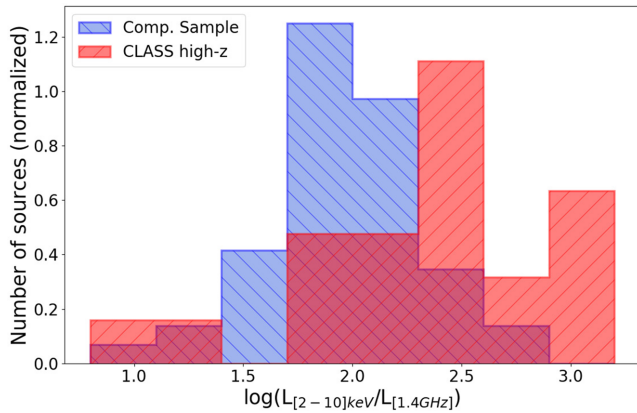
Figure 7. Distribution of the ratio between the X-ray [2–10] keV and the radio 1.4 GHz rest-frame luminosities for both the CLASS sample (red) and the comparison sample of blazars at lower redshift, $\bar{z} \sim 1.1$ (blue).

As anticipated in Ighina et al. (2018), we find a discrepancy between the distribution of low-z and high-z blazars, in particular, the clear shift between the two peaks in Fig. 7 suggests that either CLASS blazars have a stronger X-ray emission, or they have a fainter radio emission than low-z blazars. In order to quantify the difference in the two distributions we used the Kolmogorov–Smirnov test (KS test) on both samples. According to this test, the probability that the two samples belong to the same 'family', i.e. their distributions are drawn from a common one, is <0.001 per cent. In particular, the difference between the mean values of the distributions indicates that the CLASS blazars have X/R ratios ~2.4 ± 0.5 times higher than low-z blazars. Moreover we want to stress that this discrepancy is not a selection effect related to the limit imposed on the X-ray-to-optical luminosity ratio in our classification. Indeed this difference in the two distributions would still be significant (<0.001 per cent) even considering all the sources present in the CLASS regardless to our classification as blazar and non-blazars.

A similar trend has been observed also by Wu et al. (2013) and Zhu et al. (2019), in a population of very radio-loud AGN (log $R > 2.5$, some in common with this work). In both works it was found a significant difference (a factor $1.9^{+0.5}_{-0.4}$ in Zhu et al. 2019) in the X-ray-to-optical luminosity ratio. Wu et al. (2013) proposed as possible explanation for this trend a fractional IC/CMB model for the X-ray emission of blazars. The photons from the CMB are expected to interact via Inverse Compton (IC) scattering with the relativistic electrons in the jet producing emission in the X-rays (e.g. Harris & Grindlay 1979), thus enhancing the total observed X-ray luminosity. This interaction is negligible in the compact innermost regions of the jet (e.g. Ghisellini & Tavecchio 2009), but it is expected to be important for the electrons located in extended part of the jet (at few kpc), becoming negligible again at greater distances due to the deceleration of the jet (e.g. Marshall et al. 2018). According to this model, only a fraction of the X-ray emission observed at low redshifts is due to this interaction, the remaining being produced by IC scattering with photons produced by the AGN itself (e.g. accretion disc, broad-line region, dusty torus, etc...). Since the density of the CMB increases as $(1 + z)^4$ the interaction with these photons is expected to become more and more important at high redshifts (e.g. Schwartz 2002), thus producing an X-ray luminosity comparable (or even stronger) to the emission coming from the most compact region. This could explain why high-z blazars have, on average, X-ray luminosities larger than low-z blazars. In particular, following Wu et al. (2013), we expect that:

$$\frac{L_X}{L_R}(z) = \frac{L_X}{L_R}(z = 0)\left[1 + A(1 + z)^4\right], \qquad (2)$$

where A is the fraction between the extended and the compact emission at $z = 0$. In order to obtain an enhancement similar to the one observed in our sample we need $A \approx 1.6 \times 10^{-3}$, corresponding to a contribution of about 4 per cent at $z = 1.3$, similar to the values found in Wu et al. (2013) and Zhu et al. (2019). In order to firmly test this interpretation, the observation and the study of the blazars in different ranges of redshift (especially at $z > 5.5$) are necessary. It is worth noting that this effect, if present, may alter the classification

of some sources made in Section 5, in particular those with a value of $\tilde{\alpha}_{ox}$ close to the threshold, leading to the misclassification of some RL AGNs as blazars due to their enhancement of the X-ray emission. After correcting the values of the $\tilde{\alpha}_{ox}$ for the additional X-ray emission related to the CMB, there are five sources here classified as blazar that would overcome the threshold. For this reason, we mark the X-ray classification of these objects in Table 3 with a '?'. In any case, as already explained above, a change of classification of these sources would have a negligible impact on the analysis presented here.

Using the sources classified as blazar according to their radio spectrum, C19 were able to infer the space density of blazars at $z > 4$. Even adopting the new blazar classification, based on the X-ray data, the space density discussed in C19 does not change significantly. In particular, C19 found that the space density of blazars at $z > 4$, including the most luminous ones, is consistent with a density evolution peaking at $z \sim 2$, as suggested by Mao et al. (2017). This is in apparent contrast with the results presented by Ajello et al. (2009) based on a sample of X-ray selected blazars (Swift-BAT), according to which the most (X-ray) luminous objects present a peak at much higher redshifts ($z \sim 4$). In principle, this discrepancy could be explained by an evolution of the X-ray-to-radio luminosity ratio with redshift like the one discussed here. However, the X-ray-to-radio luminosity ratios observed in the highest redshift blazars of the Ajello et al. (2009) sample ($2 < z < 3$) are even larger than the one observed in the CLASS $z > 4$ blazars, something that does not seem to be consistent with the CMB model, according to which the X-ray-to-radio flux ratio should monotonically increase with redshift. Either the observed dependence of the X-ray-to-radio luminosity ratio with redshift is not due to the interaction with the CMB or its impact is not the same in all the sources. For instance, if the value of the parameter A is not unique, but it follows (as reasonable) a distribution of values, we expect that the X-ray selected blazars at redshift 2–3 constitute the (small) tail of the population with a significantly larger value of A (~ 0.01–0.1), where the enhancing effect of the CMB has a major role. The presence of these few, but extreme sources, would affect the evolution estimate based on the BAT survey, suggesting a density peak at very large redshift (~ 3–4). We are running detailed simulations to test the validity of this scenario.

7 CONCLUSIONS

In this work we presented the X-ray properties of the CLASS sample of blazar candidates discussed in C19. In order to have a reliable classification of all blazars, we performed an X-ray analysis of their *Chandra*, *XMM-pn*, and *Swift-XRT* observations. In order to classify these sources according to the intensity and the flatness of their X-ray spectra, we re-defined the commonly used α_{ox} parameter, using a higher X-ray energy, 10 keV instead of 2 keV, that was more suited for low-z sources. We then used a sample of confirmed blazars at lower redshift and one of RQ AGNs at redshift similar to the CLASS sample to estimate the limits on the photon index and the $\tilde{\alpha}_{ox}$ for the classification. We concluded that 21 sources of the CLASS sample have an X-ray emission consistent with a blazar nature, whereas the remaining three are too faint to be blazars.

Finally, we compared the CLASS high-z blazars with a sample of blazars selected at lower redshift ($z \sim 1$). In particular, we found a dependence in the class of blazars of the X/R emission ratio on the redshift. Following Wu et al. (2013) we interpret this difference as due to the interaction of the electrons in relatively extended (a few kpc) regions of the jet with CMB photons through IC. A high angular resolution radio campaign is under way in order to strengthen the blazar classification of the sources and to study of the inner part of the radio jet.

REFERENCES

Ajello M. et al., 2009, ApJ, 699, 603
Bassett L. C., Brandt W. N., Schneider D. P., Vignali C., Chartas G., Garmire G. P., 2004, AJ, 128, 523
Belladitta S., Moretti A., Caccianiga A., Ghisellini G., Cicone C., Sbarrato T., Ighina L., Pedani M., 2019, A&A, in press
Browne I. W. A. et al., 2003, MNRAS, 341, 13
Burrows D. N. et al., 2005, Space Sci. Rev., 120, 165
Caccianiga A. et al., 2019, MNRAS, 484, 204(C19)
Cash W., 1979, ApJ, 228, 939
Chambers K. C. et al., 2016, preprint (arXiv:1612.05560)
Cheung C. C., Stawarz L., Siemiginowska A., Gobeille D., Wardle J. F. C., Harris D. E., Schwartz D. A., 2012, ApJ, 756, L20
Condon J. J., Cotton W. D., Greisen E. W., Yin Q. F., Perley R. A., Taylor G. B., Broderick J. J., 1998, AJ, 115, 1693
Coppejans R. et al., 2017, MNRAS, 467, 2039

Donato D., Ghisellini G., Tagliaferri G., Fossati G., 2001, A&A, 375, 739

Eitan A., Behar E., 2013, ApJ, 774, 29

Evans P. A. et al., 2009, MNRAS, 397, 1177

Galbiati E. et al., 2005, A&A, 430, 927

Garmire G. P., Bautz M. W., Ford P. G., Nousek J. A., Ricker G. R., Jr., 2003, in Truemper J. E., Tananbaum H. D., eds, Proc. SPIE Conf. Ser. Vol. 4851, X-Ray and Gamma-Ray Telescopes and Instruments for Astronomy. SPIE, Bellingham, p. 28

Ghisellini G., Tavecchio F., 2009, MNRAS, 397, 985

Ghisellini G., Tavecchio F., Foschini L., Ghirlanda G., Maraschi L., Celotti A., 2010, MNRAS, 402, 497

Ghisellini G., Sbarrato T., Tagliaferri G., Foschini L., Tavecchio F., Ghirlanda G., Braito V., Gehrels N., 2014, MNRAS, 440, L111

Giommi P. et al., 2019, preprint (arXiv:1904.06043)

Gregory P. C., Scott W. K., Douglas K., Condon J. J., 1996, ApJS, 103, 427

Grupe D., Mathur S., Wilkes B., Osmer P., 2006, AJ, 131, 55

Harris D. E., Grindlay J. E., 1979, MNRAS, 188, 25

Healey S. E. et al., 2008, ApJS, 175, 97

Ighina L. et al., 2018, Contribution to the 13th Italian meeting on AGN, Milan Oct 2018, Zenodo. http://doi.org/10.5281/zenodo.1475236

Intema H. T., Jagannathan P., Mooley K. P., Frail D. A., 2017, A&A, 598, A78

Kellermann K. I., Sramek R., Schmidt M., Shaffer D. B., Green R., 1989, AJ, 98, 1195

Lane W. M., Cotton W. D., van Velzen S., Clarke T. E., Kassim N. E., Helmboldt J. F., Lazio T. J. W., Cohen A. S., 2014, MNRAS, 440, 327

Mao P., Urry C. M., Marchesini E., Landoni M., Massaro F., Ajello M., 2017, ApJ, 842, 87

Marshall H. L. et al., 2018, ApJ, 856, 66

Massaro E., Maselli A., Leto C., Marchegiani P., Perri M., Giommi P., Piranomonte S., 2015, Ap&SS, 357, 75

Myers S. T. et al., 2003, MNRAS, 341, 1

Orienti M., Dallacasa D., Stanghellini C., 2007, A&A, 475, 813

Orienti M., Dallacasa D., Stanghellini C., 2010, MNRAS, 408, 1075

Page K. L., Reeves J. N., O'Brien P. T., Turner M. J. L., 2005, MNRAS, 364, 195

Pietsch W. et al., 2003, A&A, 365, L18

Romani R. W., Sowards-Emmerd D., Greenhill L., Michelson P., 2004, ApJ, 610, L9

Saez C., Brandt W. N., Shemmer O., Chomiuk L., Lopez L. A., Marshall H. L., Miller B. P., Vignali C., 2011, ApJ, 738, 53

Sbarrato T. et al., 2012, MNRAS, 426, L91

Sbarrato T., Ghisellini G., Nardini M., Tagliaferri G., Greiner J., Rau A., Schady P., 2013, MNRAS, 433, 2182

Sbarrato T., Ghisellini G., Tagliaferri G., Foschini L., Nardini M., Tavecchio F., Gehrels N., 2015, MNRAS, 446, 2483

Schwartz D. A., 2002, ApJ, 571, L71

Shemmer O., Brandt W. N., Vignali C., Schneider D. P., Fan X., Richards G. T., Strauss M. A., 2005, ApJ, 630, 729

Shemmer O. et al., 2006, ApJ, 644, 86

Siemiginowska A., Smith R. K., Aldcroft T. L., Schwartz D. A., Paerels F., Petric A. O., 2003, ApJ, 598, L15

Steffen A. T., Strateva I., Brandt W. N., Alexander D. M., Koekemoer A. M., Lehmer B. D., Schneider D. P., Vignali C., 2006, AJ, 131, 2826

Tananbaum H. et al., 1979, ApJ, 234, L9

Vanden Berk D. E. et al., 2001, AJ, 122, 549

Vignali C., Brandt W. N., Schneider D. P., Garmire G. P., Kaspi S., 2003, AJ, 125, 418

Volonteri M., 2010, A&AR, 18, 279

Volonteri M., Haardt F., Ghisellini G., Della Ceca R., 2011, MNRAS, 416, 216

Worsley M. A., Fabian A. C., Celotti A., Iwasawa K., 2004, MNRAS, 350, L67

Wright E. L. et al., 2010, AJ, 140, 1868

Wu J., Brandt W. N., Miller B. P., Garmire G. P., Schneider D. P., Vignali C., 2013, ApJ, 763, 109

York D. G. et al., 2000, AJ, 120, 1579

Yuan W., Fabian A. C., Celotti A., Jonker P. G., 2003, MNRAS, 346, L7

Yuan W., Fabian A. C., Worsley M. A., McMahon R. G., 2006, MNRAS, 368, 985

Zeimann G. R., White R. L., Becker R. H., Hodge J. A., Stanford S. A., Richards G. T., 2011, ApJ, 736, 57

Zhu S. F., Brandt W. N., Wu J., Garmire G. P., Miller B. P., 2019, MNRAS, 482, 2016

This paper has been typeset from a TeX/LaTeX file prepared by the author.